PRE-driven protein NMR structures: an alternative approach in highly paramagnetic systems

Inês B. Trindade[1] iD, Michele Invernici[2] iD, Francesca Cantini[2] iD, Ricardo O. Louro[1] iD and Mario Piccioli[2] iD

1 Instituto de Tecnologia Química e Biológica António Xavier (ITQB-NOVA), Universidade Nova de Lisboa, Oeiras, Portugal
2 Magnetic Resonance Center and Department of Chemistry, University of Florence, Sesto Fiorentino, Italy

Metalloproteins play key roles across biology, and knowledge of their structure is essential to understand their physiological role. For those metalloproteins containing paramagnetic states, the enhanced relaxation caused by the unpaired electrons often makes signal detection unfeasible near the metal center, precluding adequate structural characterization right where it is more biochemically relevant. Here, we report a protein structure determination by NMR where two different sets of restraints, one containing Nuclear Overhauser Enhancements (NOEs) and another containing Paramagnetic Relaxation Enhancements (PREs), are used separately and eventually together. The protein PioC from *Rhodopseudomonas palustris* TIE-1 is a High Potential Iron-Sulfur Protein (HiPIP) where the [4Fe-4S] cluster is paramagnetic in both oxidation states at room temperature providing the source of PREs used as alternative distance restraints. Comparison of the family of structures obtained using NOEs only, PREs only, and the combination of both reveals that the pairwise root-mean-square deviation (RMSD) between them is similar and comparable with the precision within each family. This demonstrates that, under favorable conditions in terms of protein size and paramagnetic effects, PREs can efficiently complement and eventually replace NOEs for the structural characterization of small paramagnetic metalloproteins and *de novo*-designed metalloproteins by NMR.

Databases

The 20 conformers with the lowest target function constituting the final family obtained using the full set of NMR restraints were deposited to the Protein Data Bank (PDB ID: 6XYV). The 20 conformers with the lowest target function obtained using NOEs only (PDB ID: 7A58) and PREs only (PDB ID: 7A4L) were also deposited to the Protein Data Bank. The chemical shift assignments were deposited to the BMRB (code 34487).

Introduction

Metalloproteins represent 40 to 47% of all known enzymes [1,2] and, for all of them, the metal center(s) are essential for catalysis, electron transfer, and metal storage/transport, or they play a crucial role in determining stability and structural properties [3–12]. Structural biologists are mainly interested in obtaining detailed information in the proximity of the metal center(s), where the biochemically relevant events occur.

NMR is a privileged approach for characterizing metalloproteins since it can provide the structure in solution at atomic resolution, information about the amplitudes and time-scales of internal dynamics [13–15], as well as hints on the electronic structure and oxidation states of the metal center [16] in conditions that mimic the physiological context. A significant part of the metallo-proteome contains paramagnetic metal ions. Their presence perturbs the chemical shift and relaxation of NMR signals in ways that can be converted into structural and dynamic information [17,18].

Early attempts to convert paramagnetic nuclear relaxation rates in NMR restraints and include them into solution structure protocols achieved the first solution structures of paramagnetic proteins [19]. The introduction of residual dipolar couplings (RDCs) arising from self-oriented paramagnetic proteins [20] combined with pseudocontact shifts (PCS) and cross-correlation rates (CCR) succeeded, in the case of cytochrome c', to obtain the first backbone structure of a protein in the absence of NOE measurements [21] and, at the same time, opened the possibility to use orientational restrains also in diamagnetic proteins. Nitroxide radicals used as site-directed spin labels allowed the conversion of Paramagnetic Broadening Effects into distance restraints for large molecular weight proteins [22]. This work led to the introduction of the 'concept' of Paramagnetic Relaxation as long-range restraints for non-native metalloproteins and the acronym PRE (Paramagnetic Relaxation Enhancements) was coined [23]. Since they are long-range constraints, PREs are a good alternative/complement to RDCs to obtain solution structures when NOES and scalar couplings are unable/insufficient to define the structure. Extrinsic paramagnetic centers can be attached via conjugation to specific, solvent-exposed sites [24] and, indeed, the use of PRE soon flourished. Macromolecular structures using PRE data have been characterized not only for soluble proteins [23,25], but also for protein–protein [26–28] and protein–nucleic acid complexes [29–31], membrane proteins [32], unfolded, or partially unfolded states [33–36], proteins in living cells [37,38]. Also in solid state protein NMR spectroscopy, PREs coupled with PCS [39,40] provided accurate solid state structures in the absence of conventional distance or dihedral angle restraints [41,42] as well as information on the oligomerization interface of large membrane proteins [43]. Actually, applications of PREs go beyond their use as structural constraints for obtaining 'static' NMR structures: They may unravel structural information on transient, invisible, intermediates [44] and provide information on encounter complexes [45–47], interdomain motions [48], transient protein

associations [49–51], nonspecific protein–DNA interactions [52] and also in drug discovery [53–56].

However, several aspects, such as the accuracy of PRE data [57] and the weak correlation observed between distance derived PREs and those found in crystallographic structures [58,59] deserve further investigations. For example, it has been shown for lanthanide ions that magnetic anisotropy provides a substantial angular dependence of nuclear relaxation rates [60,61]. Nonspecific intermolecular PREs and cross-correlations between Curie Spin Relaxation and dipolar spin–spin couplings [62,63] might be responsible for the deviation of paramagnetic relaxation rates from the r^{-6} dependency (r being the metal-to-nucleus distance) [58]. These factors limit the accuracy of PREs especially at longer metal-to-proton distances; on the other hand, at shorter metal-to-proton distances, the paramagnetism-induced line broadening prevents the detection of NMR signals limiting the information available at the close proximity of the paramagnetic center.

For the above reasons, small-sized metalloproteins are interesting cases to study the behavior of paramagnetic relaxation when the paramagnetic center is not affected by local mobility and represents the crucial part of the protein. Moreover, tailored experiments increased the availability of PRE values also at shorter metal-to-nucleus distances [64]. In these conditions, PREs are usable not only as long-range restraints but also as medium and short-range restraints. A $[Fe_4S_4]^{2+}$ cluster possesses a negligible magnetic anisotropy and it is buried within the protein. This rules out the many effects that give rise to relaxation anisotropy. Therefore, PioC, a small (54 aa residues) HiPIP (High Potential Iron Protein) from *R. palustris* TIE-1 represents a peculiar and interesting system to assess nuclear relaxation properties, analyze the relative contribution of NOE and PREs and discuss the use of PREs as alternative to NOE for the portion of the protein where the presence of paramagnetic metal ions poses a challenge for the detection of classical structural restraints and even for signal detection [21].

The interplay between NOEs and paramagnetism-based restraints has been addressed by many groups, and there are many evidences of the fact that the replacement of NOEs with other restraints is feasible, when the alternative restraints considered, arise from different complementary sources [65–68]. Sparse NOE and chemical shifts can be used together with sophisticated modeling methods to obtain well-defined solution structures [69,70]. Protein structures have also been determined without NOEs using orientational restraints from at least two full sets of RDC

[21,71–73]. Tagging a protein with lanthanide ions at four different sites succeeded to obtain a backbone structure without NOEs [74], whereas the use of different lanthanide ions on a single metal center required a minimal number of NOEs to obtain a structure [75]. A backbone structure was obtained using a combination of PRE, RDC, PCS, CCR, and backbone NOEs, which were used to properly define α helices [76]. Paramagnetic Relaxation Enhancements (PRE) are dipole–dipole restraints, like NOEs. Therefore, if a sufficient number of PRE restraints are available throughout the entire protein, they should restrain the conformational space with efficiency comparable to NOEs, even when, like in a metalloprotein, the distance restraints all involve a single point, that is, the native paramagnetic center of the system. To explore these issues, the NMR solution structure of the small iron–sulfur protein PioC from *R. palustris* TIE-1 [77] was pursued as a paradigmatic challenge. PioC mediates the electron transfer between the reaction center and the iron-oxidase in the photoferrotrophic metabolism of *R. palustris* TIE-1. It contains a [4Fe-4S] cluster with a very high reduction potential ($E^0 = +450$ mV vs SHE), being stable in the $[Fe_4S_4]^{2+}$ oxidation state. With 54 amino acids, it is the smallest HiPIP ever isolated. Its 3D structure is unknown, but homology modeling with other HiPIPs suggests that the protein has a compact globular structure, characterized by the absence of topologically relevant secondary structure elements; it is instead predicted to be composed essentially by a series of loops and turns wrapped around the [4Fe-4S] cluster [78,79]. The electronic properties of $[Fe_4S_4]^{2+}$ in HiPIPs have been studied in detail over the past 40 years [3,80-88]. The magnetic coupling within the [4Fe-4S] cluster makes the electronic correlation times of the individual iron ions much shorter than isolated high spin Fe^{3+} or Fe^{2+} ion; nevertheless, paramagnetic contributions to nuclear relaxation are significant for nuclei within a 10 Å sphere from the cluster [89,90]. Therefore, PioC is a suitable system to address an important issue for inorganic biochemistry: Is it possible to improve methods for measuring relaxation rates in paramagnetic systems to the point that PREs can be used as the sole source of restraints to define the structure of a metalloprotein?

Results and Discussion

NMR experiments currently available for measuring ^1H R_1 and R_2 rates [23,57] fail to provide PRE data in the proximity of the paramagnetic center, where many signals are broadened beyond detection. This limits the use of PREs in metalloproteins, in which

the paramagnetic center is also the core of the protein. Recently, we developed experiments [64,91] that provided accurate ^1H R_1 and R_2 values in the range 50–500 s^{-1} and substantially improved the amount of PRE restraints in the close proximity of the paramagnetic center. Accurate measurements of both R_1 and R_2 rates are important to obtain reliable information on the metal-to-proton distances and to use PREs also as short-range restraints. A standard ^{15}N HSQC experiment on a PioC sample shows only 39 amide resonances out of expected 49 non-proline residues. However, a ^{15}N IR-HSQC-AP experiment, specifically designed to observe fast relaxing resonances, shows additional 10 resonances, demonstrating that all H_N signals of PioC can be detected (Fig. 1A).

The complete resonance assignment of the protein was obtained combining the conventional approach based on triple resonance experiments (Table S1) with a non-systematic procedure using a combination of 1D NOEs, ^{13}C direct detection, double and triple resonance experiments recorded with parameters optimized à-la-carte (Table S2) [92]. These experiments provided the complete NMR assignment of PioC (BRMB entry 34487) [93]. We assigned (excluding the N-ter Val 1) 100% of backbone ^1H_N, ^{13}C, and ^{15}N resonances, 98% of Hα, 86% and 91% of ^1H and ^{13}C side chains atoms, respectively. However, even though the ^1H resonance were almost completely assigned, ^{15}N and ^{13}C HSQC-NOESY experiments at high magnetic field gave only 344 meaningful NOEs, that without any additional information on the [4Fe-4S] cluster binding mode, were insufficient to obtain a converged structure. Three factors quench these NOE intensities: (i) the small rotational correlation time (3.4×10^{-9} s, from ^{15}N relaxation); (ii) paramagnetic relaxation affecting at least 50% of the protein; and (iii) the absence of secondary structure elements, typical of HiPIPs. We introduced the cluster into structure calculations: bond distances and angles defining the geometry of the cubane cluster, that are not accessible via NMR, are given by introducing a special residue into the CYANA library [94], as described in Supporting Information. The introduction of the cluster gave structures with backbone and heavy atoms RMSD of 1.27 ± 0.20 Å and 1.95 ± 0.20 Å. Indeed, the cluster is the essential structural element to drive the fold of the polypeptide chain.

Paramagnetic NMR experiments provided structural constraints for cluster-binding residues (through coordinative or hydrogen bonds) crucial to define their orientation: Cys βCH$_2$ hyperfine shifts were converted into four χ^2 dihedral angle constraints
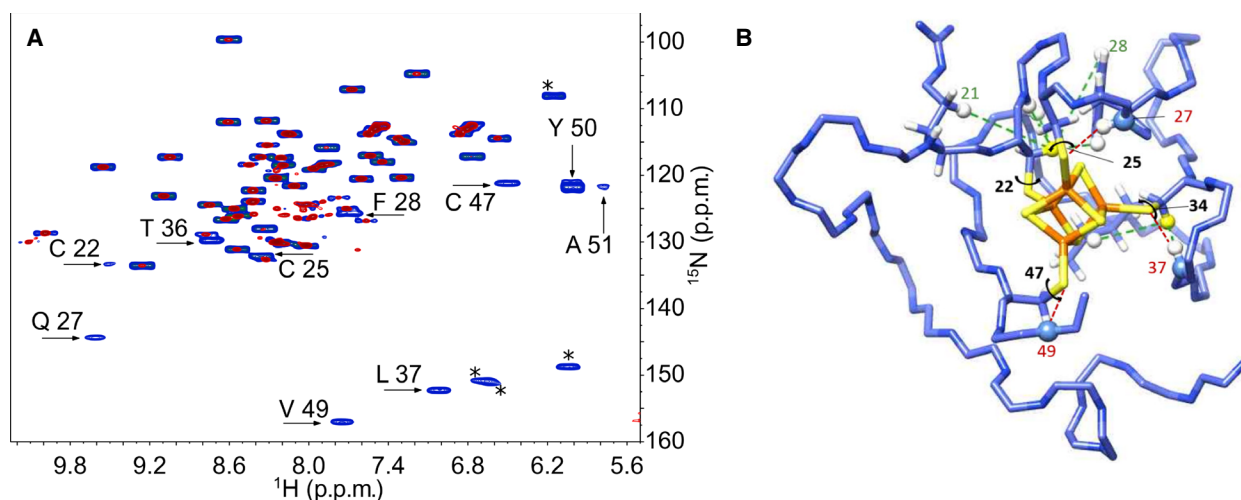
Fig 1. (A) 500 MHz 298K, ^{15}N- HSQC spectrum on PioC collected using the HSQC-AP experiment (blue), overlaid with a standard ^{15}N HSQC spectrum (red). Labeled signals are observable only in the HSQC-AP spectrum. Signals marked with asterisks are folded peaks arising from side chains. (B) Cluster-derived NMR restraints: dihedral angles χ^2 of cluster-bound Cysteines (black), hydrogen bonds between HN residues and Sγ of Cysteines (red), ^{1}H NOEs between well-resolved ^{1}H βCH$_2$ Cys resonances and surrounding protons (green). Molecular graphics performed with UCSF Chimera, developed by the Resource for Biocomputing, Visualization, and Informatics at the University of California, San Francisco, with support from NIH P41-GM103311.

defining the cluster binding topology according to a procedure already described [95], seven crucial 1D NOEs provided distances between Cys βCH$_2$ and neighboring residues (Fig. S1), large ^{15}N contact shifts, observed for Gln27, Val37, and Leu49 [93] were taken as an evidence of three hydrogen bonds, respectively, linking H$_N$ to the Sγ atoms of the preceding (i-2 or i-3) cluster-bound cysteine residues [96]. Only fourteen constraints of this type are available but they are extremely important to frame the cluster within the protein and to provide restraints where other experimental approaches fail to provide information. These cluster-derived restraints are shown in Fig. 1B. When also these constraints were
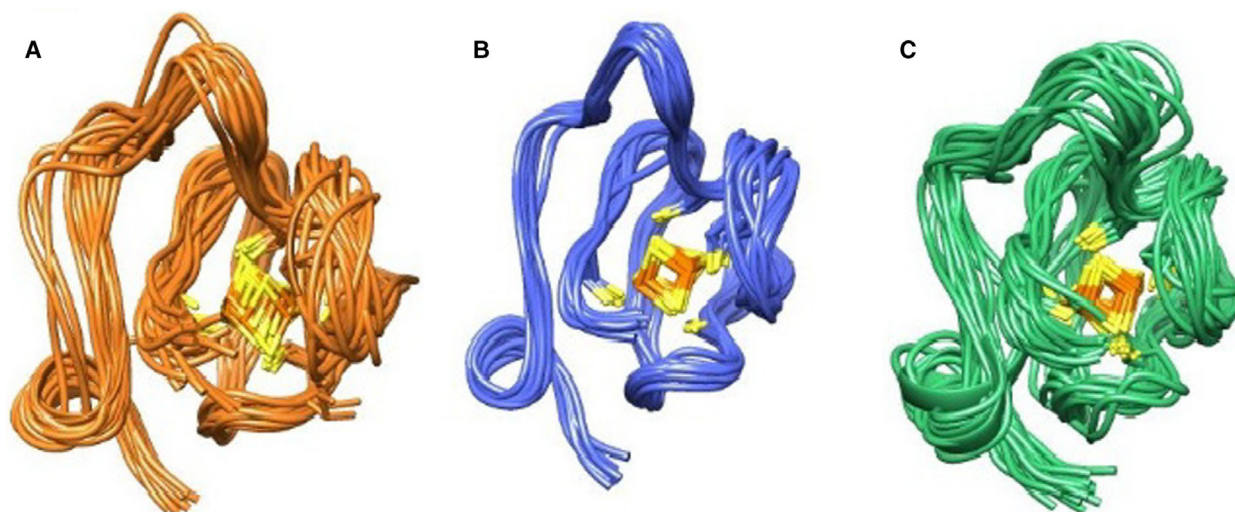

Fig 2. Solution structure of PioC obtained using NOEs only (orange), the full set of NMR restraints (blue), PREs only (green). In all cases, the families of 20 conformers were obtained from Torsion Angle Dynamics (CYANA2.1) and refinement using molecular dynamics (AMBER-16 package). Residues 5–49 are shown. Molecular graphics performed with UCSF Chimera.
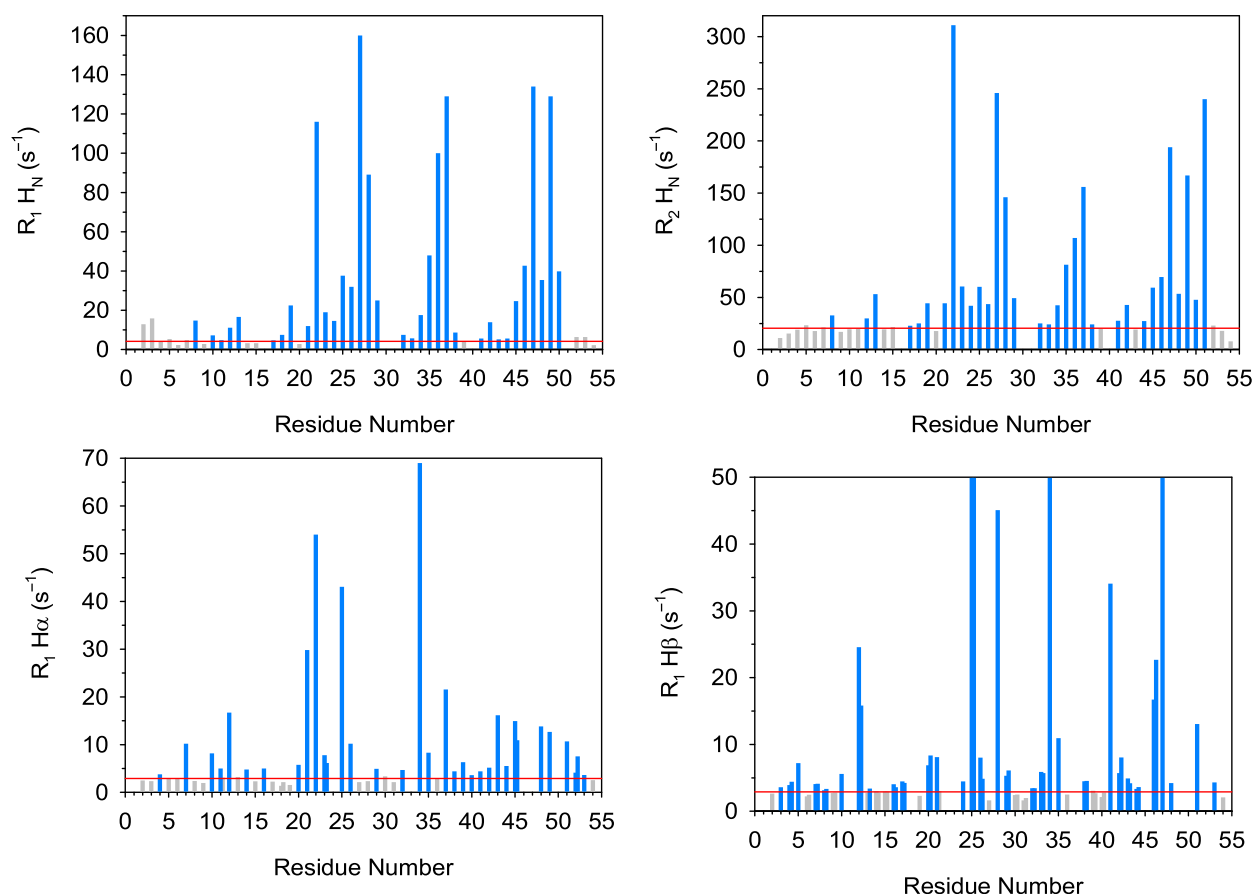
Fig 3. Longitudinal and transverse relaxation rates of amide and aliphatic protons. Horizontal red lines show the average diamagnetic values. Blue histograms are rates converted into PRE values. Values of Hβ are out of scale (see Table S3).

included into structure calculation, a well-converged structure was obtained (Fig. 2A), with backbone and heavy atoms RMSD of 1.04 ± 0.30 Å and 1.81 ± 0.30 Å (residues 5–50).

We next considered the impact of PREs: To this end, we collected R_1 and R_2 values of all amide protons using the ^{15}N-IR-HSQC-AP (48 ^{1}H R_1 values) and the R_2-weighted ^{15}N-HSQC-AP experiments (50 ^{1}H R_2 values) [64]. For non-exchangeable protons, a ^{13}C-IR-HSQC-AP provided R_1 values of 200 ^{1}H protons of backbone ^{1}Hα and side chains. Finally, ^{1}H and ^{13}C resonances of cluster-bound Cys residues, identified and assigned using rapid recycling experiments, provided thirteen R_1 and R_2 values from inversion recovery and linewidth analysis of one dimensional ^{1}H and ^{13}C experiments. Overall, 306 ^{1}H (amide protons plus backbone ^{1}Hα and aliphatic side chains) and 5 ^{13}C relaxation rates, amounting to ca. six rates per residue, were measured (Table S3). The behavior of

H_N, Hα, and Hβ rates is shown in Fig. 3 and points out that about 60 % of signals are affected by the paramagnetic center.

The $R_{1,2para}$ contributions are calculated according to:

$$R_{1,2obs} = R_{1,2dia} + R_{1,2para} \qquad (1)$$

For backbone atoms, $R_{1,2dia}$ (red lines in Fig. 3) were estimated from averaged values of residues 4–7, that do not belong to the flexible N-term loop (Fig. S2) and are not affected by paramagnetism. For side chains protons, the R_{1dia} values were taken by considering for each type of proton, the average value obtained by taking into account only values within the standard deviation. Then, $R_{1,2 \ para}$ (blue histograms in Fig. 3) are converted into distances (r_{MH}) according to the Solomon–Bloembergen equations [97]

$$R_1 = \frac{2}{15}\left(\frac{\mu_0}{4\pi}\right)^2 \frac{\gamma_I^2 \mu_B^2 g_e^2 S(S+1)}{r_{MH}^6}\left(\frac{\tau_c}{1+(\omega_I-\omega_S)^2\tau_c^2} + \frac{3\tau_c}{1+\omega_I^2\tau_c^2} + \frac{6\tau_c}{1+(\omega_I+\omega_S)^2\tau_c^2}\right) \tag{2}$$

$$R_2 = \frac{1}{15}\left(\frac{\mu_0}{4\pi}\right)^2 \frac{\gamma_I^2 \mu_B^2 g_e^2 S(S+1)}{r_{MH}^6}\left(4\tau_C\frac{\tau_c}{1+(\omega_1-\omega_S)^2\tau_c^2} + \frac{3\tau_c}{1+\omega_1^2\tau_c^2} + \frac{6\tau_c}{1+(\omega_1+\omega_S)^2\tau_c^2} + \frac{6\tau_c}{1+\omega_S^2\tau_c^2}\right)$$
$$+ \frac{1}{5}\left(\frac{\mu}{4\pi}\right)^2\left(\frac{\omega_1^2\mu_B^2 g_e^2 S^2(S+1)^2}{(3kT)^2 r_{MH}^6}\right)\left(4\tau_r + \frac{3\tau_r}{1+\omega_I^2\tau_r^2}\right) \tag{3}$$

In the equations, we considered $\tau_c = 6 \times 10^{-12}$ s, arising from an estimated value of τ_e for each iron ion, $\tau_r = 3 \times 10^{-9}$ s obtained from ^{15}N relaxation, and $S = 1$, arising from the lowest excited state of the electron spin ladder of the $[Fe_4S_4]^{2+}$ cluster. Distances obtained from eqs (2 and 3) were then converted into upper limit distances (upl). For non-exchangeable protons, we obtained overall 122 upl. For amide HN resonances, when R_1 and R_2 provided different upper distance limits for the same ^1H_N proton, the upper limit value was taken by considering the less restrictive value among the two. In these cases, the upper limit value was given a weighting factor 2. For the 49 non-proline residues, 30 upper distance limits were used.

Since we do not have *a priori* the information on which iron of the cluster is causing the dipole coupling with each nucleus, in a first structure calculation all PRE-based upper limit distance restraints were assigned to the mass center of the cluster, rather than to a specific iron ion of the cluster. This was obtained by adding at the end of the protein sequence a special linker made of 100 pseudo-residues called LL2. The 'atoms' of LL2 pseudo-residues have zero mass and zero van der Waals radii, thus the linker can freely pass through the structure during simulated annealing. The last residue of the linker is an ION residue (CYANA library) which has been subsequently linked at fixed distances with the four iron ions and with the four sulfur ions of the cluster, with van der Waals contact taken to zero in order to avoid distortions or additional contribution to the overall energy. In this construct, the ION residue represents therefore the mass center of the cubane. Additional 1.4 Å (where 1.4 Å is the distance between each iron and the mass center of the cubane in the typical [4Fe-4S] structure) was added to all upl values obtained from PREs and all restraints were given to the center of mass of the cubane. To perform the final refinement via AMBER,

for each PRE restraint the center of mass of the cubane has been replaced with the closest iron ion of the cluster as resulting from the structure obtained with CYANA (or with the two closest iron ions when ambiguous metal-to-proton distances occur) and the upper limit distance taken from eqs (2 and 3).

Paramagnetic relaxation enhancements that are violated in a significant number of structures were critically analyzed, taking also into account the NOES. It was found that, while no violations have been observed for PREs obtained from non-exchangeable protons, some of the PRE values of exchangeable H_N gave rise to consistent violations. Some of them are due to local internal dynamics (^{15}N relaxation shown in Fig. S2). However, some of the R_1 and R_2 H_N values belonging to the residues 5–20 (i.e., the N-terminal part preceding the cluster-binding region) and to residues 42–44 (part of the long loop between Cys 34 and Cys 47) showed consistent violations that are not accounted by ^{15}N relaxation. All these residues have calculated iron-to-proton distances in the range 7–11 Å, while no violations were observed for H_N distances in the range 4–7 Å. This effect is observed only for exchangeable amide protons; indeed, aliphatic protons values were in very good agreement with the structure also at distances > 10 Å. This suggests that magnetic susceptibility anisotropy is not the only factor responsible for the deviation from eqs 2 and 3 [58,61], as also previously observed in Cu(II) proteins [59]. Intermolecular effects and/or solute–solvent interactions could be possible factors affecting the quantitative analysis of H_N relaxation rates. PREs giving rise to consistent violations were excluded from structure calculation. Overall, 175 PRE restraints were retained from relaxation-rate data (Table S4), and the total number of distance restraints (NOE and PRE) was increased to 533. A summary of these restraints is reported in Table S5.

The addition of relaxation-based NMR restraints gave a more tightly converged NMR structure, with backbone and side chain RMSD values of 0.62 ± 0.11Å and 1.14 ± 0.13Å, respectively (Fig. 2B). PRE data improved the quality of the structure not only in the proximity of the cluster, but throughout the entire protein. The combination of both type of restraints led to statistical parameters that are indicative of a highly precise structure of a well-folded protein of small/medium size (Table S6). Finally, we addressed the question of whether an NMR structure obtained without NOEs is able to achieve good accuracy and precision. Figure 2C shows the family of structures obtained without the 344 NOEs from ^{13}C and ^{15}N-NOESY-HSQC experiments. The structure has backbone and heavy atoms RMSD of 1.31 ± 0.27Å and 2.00 ± 0.32Å, respectively. The

overall precision is obviously lower than that obtained with the full set of restraints and it is also lower than that obtained with NOE-only, because of the lower number of restraints, but still lies within an acceptable structure quality range. The per-residue comparison of backbone RMSD (Fig. 4A) shows that the family obtained with the full set of restraints has always the lowest RMSD (except Thr24), indicating that the combination of NOEs and PREs improves the precision in all the protein regions. PREs provide information exactly were NOEs are missing, thus complementing NOE data. In several protein regions, the NOE-only family has an RMSD similar to the family obtained with the full set of restraints, indicating that NOEs drive the structure toward a minimum. Conversely, in other protein regions, the precision is improved by the use of PREs; in these regions, the structure quality is
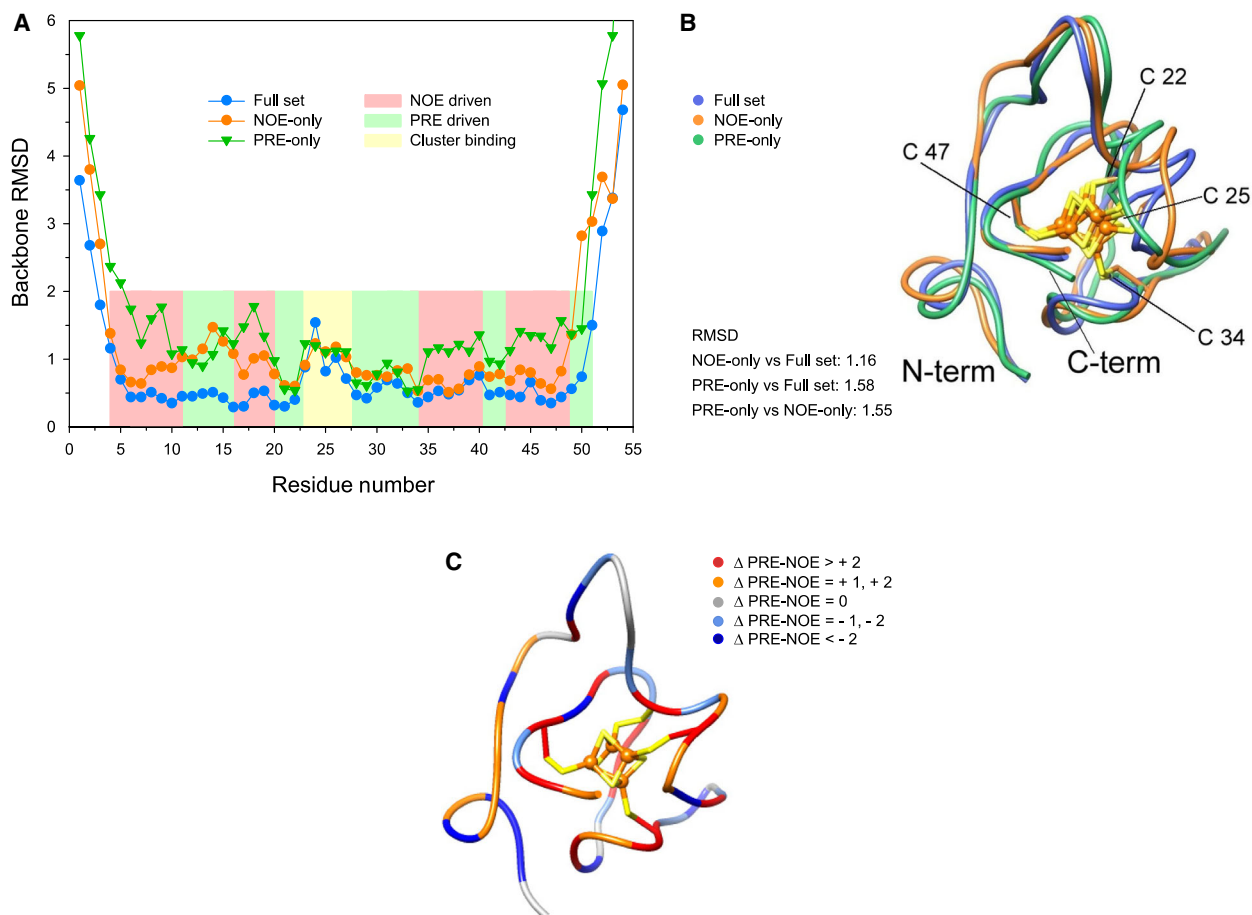
Fig 4. (A) per-residue RMSD values of the three different families. The relative contribution of the different set of constraints on a per-residue basis is shown with the color code indicated in the Figure. (B) Superimposing of the most representative structures of each ensemble obtained with different sets of constraints. Figure reports also pairwise backbone RMSD values. (C) Regions where the number of PRE restraints exceeds that of long-range NOE restraints are shown in red and orange; regions were the opposite occurs are shown in blue and light blue. Molecular graphics performed with UCSF Chimera.

PRE driven. The loop surrounding the cluster and containing Cys 22 and Cys 25 of the CXXC binding motif in HiPIPs has a different trend. Here, the RMSD values of the three families are similar and higher than average values. This is the situation in which, not only NOEs but also PREs are missing due to the close proximity to the paramagnetic center. Essentially, for this fragment the structure is given by the cluster-binding topology, by the dihedral angles of Cys bound residues, and by the hydrogen bonds identified by ^{15}N contact shift. We can obtain clues on the accuracy of the structures by comparing the most representative structures of the three families: the PRE-only, the NOE-only, and the full-set structures. As shown in Fig. 4B, the pairwise RMSD between them are all similar and comparable with the precision within each family. The representative conformer selected from the ensemble obtained with the full set of restraints is, for most of the protein, in an average position among the representative conformers of the PRE-only and NOE-only ensemble. The PRE-only structure ensemble is essentially the same, although with a larger RMSD, as the one obtained with the full set of restraints. Finally, Fig. 4C points out the relative impact of PREs vs long-range NOEs. As expected, residues surrounding the cluster have a dominance of PREs; however, also regions from a larger sphere, such as stretch 10–13, experiences the contribution of PREs. Noteworthy, an opposite behavior is observed for the aromatic residue surrounding the cluster Trp46, which experiences both NOEs and PREs. This large hydrophobic residue has the role of maintaining the hydrophobicity of the cluster and protecting it from solvent accessibility. Therefore, it gives rise to many long-range NOEs, extending from the close proximity of the paramagnetic center to the diamagnetic region.

Conclusions

Notwithstanding the exciting perspectives opened by computational biologists [98–101], the quest for novel experimental restraints remains of primary importance for structural modeling. Up to date, a dense network of NOEs has always been considered essential for NMR structures, because restraints between residues that are far apart in the primary sequence define the relative orientation of different structural motifs [102]. Factors such as protein size, electronic correlation times of metal ion(s) and internal mobility modulate the interplay between paramagnetism-based and conventional NMR restraints and their relative contribution to the final structure. The NMR structure of PioC

is a proof of concept that PREs may drive a solution structure and eventually act as the sole source of NMR restraints. When a protein is small enough to be affected by paramagnetism in a large percentage, then NOEs are not essential anymore, if relaxation rates are measured virtually for all ^{1}H spins. In PioC, the $[Fe_4S_4]^{2+}$ cluster provides upper distance limits for PREs up to 13 Å, while the average protein radius is about 15 Å, thus being an ideal case for obtaining an accurate and well-converged PRE-driven NMR structure. In this case, an extended network where all the ^{1}H spins are linked to a single point (the metal center) via long-range dipolar couplings can completely replace a network of short-range dipole–dipole ^{1}H-^{1}H couplings. The availability of PREs from aliphatic protons circumvent the lack of accuracy for long metal-to-proton distances of exchangeable protons. This represents an opportunity for the characterization and structural study of metallopeptides and *de novo*-designed and bio-inspired metalloenzymes [103–105]. These results argue for the systematic use of PREs in structure calculations of metalloproteins where metal substitution is not possible since they provide distance restraints in protein regions where NOEs are sparse due to paramagnetism, and where most biochemically relevant events occur.

Materials and methods

Protein expression and purification

E. coli BL21 DE3 cells were transformed with pET32h, a plasmid containing the construct thioredoxin–6xHis–thrombin cleavage site–PioC, and with pDB1281, a plasmid that carries the machinery for the assembly of iron–sulfur clusters. Cells were grown in Luria-Bertani (LB) supplemented with 100mg*dm^{-3} ampicillin and 35mg*dm^{-3} chloramphenicol until the OD600nm of 0.6 where they were induced with 1.0 mM arabinose and 20 μM FeCl$_3$ and 200 μM cysteine were added. Cells were again incubated until the OD600nm of 1 and then harvested and washed in M9 minimal media salts before resuspension in M9 minimal media. Once re-suspended, cells were incubated for one hour before induction with 0.5 mM IPTG. After 4 h, cells were harvested by centrifugation and disrupted using a French Press at 1000psi. The lysate was ultra-centrifuged at 204 709 g for 90 min at 4 °C to remove cell membranes and debris, and the supernatant was dialyzed overnight against 50 mM potassium phosphate buffer pH 5.8 with 300 mM NaCl before injection in a His-trap affinity column (GE Healthcare, Carnaxide, Portugal). The fraction containing Histag-PioC eluted with 250 mM imidazole and was incubated overnight with Thrombin (GE Healthcare) for digestion. The final purified PioC (His-tag free) was then

concentrated from the flow through of a 2nd passage through the His-trap column using an Amicon Ultra Centrifugal Filter (Millipore, Darmstadt, Germany) with a 3kDa cutoff. The purity of PioC was confirmed by SDS/PAGE with Blue Safe staining (NzyTech, Lisboa, Portugal) and by UV-Visible spectroscopy. Three samples of PioC were produced (unlabeled, single ^{15}N-labeled, double ^{13}C &^{15}N-labeled) and the expression and purification protocol was identical throughout except in the addition of ammonium sulfate ($^{15}N_2$, 99%) and [U-$^{13}C_6$] D-glucose in the M9 minimal media when labeling was required.

NMR experiments

All experiments were recorded using Bruker AVANCE-NEO spectrometers, equipped with cryogenically cooled triple resonance inverse detection probeheads (CP-TXI), except ^{13}C-detected experiments, which were acquired at 176.05 MHz using a cryogenically cooled probehead optimized for ^{13}C direct detection (CP-TXO), and ^1H experiments which were recorded at 400 MHz using a room temperature, selective 5mm ^1H probe without pulsed field gradients. All spectra were processed using the Bruker software TopSpin. Standard radio frequency pulses and carrier frequencies for triple resonance experiments were used. The set of NMR experiments used for sequence specific assignment, NOE collection, and ^{15}N relaxation analysis is summarized in Table S1. To identify signals affected by the hyperfine interaction, tailored experiments were performed [64,91,92]. Experimental parameters are summarized in Table S2. Data analysis and resonances assignment were performed using CARA 1.9 [106]. The complete assignment has been submitted in BRMB entry 34487 [93].

Structure calculations

Structure calculations were performed with the program CYANA 2.1 [107,108]. NOEs were analyzed and converted into upper distance limits and used for manual structure calculation in CYANA 2.1. Backbone dihedral angle constraints were derived from ^{15}N, $^{13}C'$, $^{13}C\alpha$,$^{13}C\beta$, and Hα chemical shifts, using TALOS + and added as restraints. All structure ensembles presented here were refined with molecular dynamics using AMBER-16 [109] and force field parameters for the 4Fe4S cluster as previously described [110,111] and validated using PDBstat and PSVS programs [112,113]. Detailed description of the methodology used for structure calculation and refinement is reported in supplementary material.

Acknowledgements

Author contributions

RL and MP designed research. IT, MI, FC, and MP performed research. FC, MI, and IT analyzed data; and MP, RL, FC, IT, and MI wrote the paper.

Conflict of interest

The authors declare no conflict of interest.

References

1 Andreini C, Bertini I, Cavallaro G, Holliday GL & Thornton JM (2008) Metal ions in biological catalysis: from enzyme databases to general principles. *J Biol Inorg Chem* **13**, 1205–1218.

2 Waldron KJ, Rutherford JC, Ford D & Robinson NJ (2009) Metalloproteins and metal sensing. *Nature* **460**, 823–830.

3 Beinert H (2000) Iron-sulfur proteins: ancient structures, still full of surprises. *J Biol Inorg Chem* **5**, 2–15.

4 Cai K, Liu G, Frederick RO, Xiao R, Montelione GT & Markley JL (2016) Structural/Functional properties of human NFU1, an intermediate [4Fe-4S] carrier in human mitochondrial iron-sulfur cluster biogenesis. *Structure* **24**, 2080–2091.

5 Mulliez E, Duarte V, Arragain S, Fontecave M & Atta M (2017) On the role of additional [4Fe-4S] clusters with a free coordination site in radical-SAM enzymes. *Front Chem* **5**, 17.

6 Ciofi-Baffoni S, Nasta V & Banci L (2018) Protein networks in the maturation of human iron-sulfur proteins. *Metallomics* **10**, 49–72.

7 Perard J & Ollagnier de Choudens S (2018) Iron-sulfur clusters biogenesis by the SUF machinery: close to the molecular mechanism understanding. *J Biol Inorg Chem* **23**, 581–596.

8 Freibert SA, Weiler BD, Bill E, Pierik AJ, Muhlenhoff U & Lill R (2018) Biochemical reconstitution and

spectroscopic analysis of iron-sulfur proteins. *Methods Enzymol* **599**, 197–226.

9 Rouault TA (2019) The indispensable role of mammalian iron sulfur proteins in function and regulation of multiple diverse metabolic pathways. *Biometals* **32**, 343–353.

10 Jia M, Sen S, Wachnowsky C, Fidai I, Cowan JA & Wysocki V (2020) Characterization of [2Fe-2S]-cluster-bridged protein complexes and reaction intermediates by use of robust native mass spectrometric methods. *Angew Chem Int Ed Engl* **59**, 6724–6728.

11 Adinolfi S, Puglisi R, Crack JC, Iannuzzi C, Dal Piaz F, Konarev PV, Svergun DI, Martin S, Le Brun NE & Pastore A (2017) The molecular bases of the dual regulation of bacterial iron sulfur cluster biogenesis by CyaY and IscX. *Front Mol Biosci* **4**, 97.

12 Wachnowsky C, Hendricks AL, Wesley NA, Ferguson C, Fidai I & Cowan JA (2019) Understanding the mechanism of [4Fe-4S] cluster assembly on eukaryotic mitochondrial and cytosolic aconitase. *Inorg Chem* **58**, 13686–13695.

13 Arthanari H, Takeuchi K, Dubey A & Wagner G (2019) Emerging solution NMR methods to illuminate the structural and dynamic properties of proteins. *Curr Opin Struct Biol* **58**, 294–304.

14 Bax A & Clore GM (2019) Protein NMR: boundless opportunities. *J Magn Reson* **306**, 187–191.

15 Cai K & Markley JL (2018) NMR as a tool to investigate the processes of mitochondrial and cytosolic iron-sulfur cluster biosynthesis. *Molecules (Basel, Switzerland)* **23**, 2213.

16 Piccioli M & Turano P (2015) Transient iron coordination sites in proteins: exploiting the dual nature of paramagnetic NMR. *Coord Chem Rev* **284**, 313–328.

17 Barry CD, North ACT, Glasel JA, Williams RJP & Xavier AV (1971) Quantitative determination of mononucleotide conformations in solution using lanthanide Ion shift and broading NMR probes. *Nature* **232**, 236–245.

18 Brassington JG, Williams RJP & Wright PE (1975) Assignment of the n.m.r. spectrum of iron(III) protoporphyrin IX dicyanide using paramagnetic shift and broadening probes. *J Chem Soc Chem Commun* 338–340.

19 Bertini I, Couture MMJ, Donaire A, Eltis LD, Felli IC, Luchinat C, Piccioli M & Rosato A (1996) The solution structure refinement of the paramagnetic reduced HiPIP I from *Ectothiorhodospira halophila* by using stable isotope labeling and nuclear relaxation. *Eur J Biochem* **241**, 440–452.

20 Tolman JR, Flanagan JM, Kennedy MA & Prestegard JH (1995) Nuclear magnetic dipole interactions in field-oriented proteins: information for structure determination in solution. *Proc Natl Acad Sci USA* **92**, 9279–9283.

21 Hus JC, Marion D & Blackledge M (2000) De novo determination of protein structure by NMR using orientational and long-range order restraints. *J Mol Biol* **298**, 927–936.

22 Battiste JL & Wagner G (2000) Utilization of site-directed spin labelling and high-resolution heteronuclear nuclear magnetic resonance for global fold determination of large proteins with limited nuclear overhauser effect data. *Biochemistry* **39**, 5355–5365.

23 Donaldson LW, Skrynnikov NR, Choy W-Y, Muhandiram DR, Sarkar B, Forman-Kay JD & Kay LE (2001) Structural characterization of proteins with an attached ATCUN motif by paramagnetic relaxation enhancement NMR spectroscopy. *J Am Chem Soc* **123**, 9843–9847.

24 Kosen PA (1989) Spin labeling of proteins. *Methods Enzymol* **177**, 86–121.

25 Gaponenko V, Howarth JW, Columbus L, Gasmi-Seabrook G, Yuan J, Hubbell WL & Rosevear PR (2000) Protein globl fold determination using site-directed spin and isotope labeling. *Protein Sci* **9**, 302–309.

26 Gross JD, Moerke NJ, von der Haar T, Lugovskoy AA, Sachs AB, McCarthy JEG & Wagner G (2003) Ribosome loading onto the mRNA cap is driven by conformational coupling between eIF4G and eIF4E. *Cell* **115**, 739–750.

27 Mal TK, Skrynnikov NR, Yap KL, Kay LE & Ikura M (2002) Detecting protein kinase recognition modes of calmodulin by residual dipolar couplings in solution NMR. *Biochemistry* **41**, 12899–12906.

28 Rumpel S, Becker S & Zweckstetter M (2008) High-resolution structure determination of the CylR2 homodimer using paramagnetic relaxation enhancement and structure-based prediction of molecular alignment. *J Biomol NMR* **40**, 1–13.

29 Varani L, Gunderson SI, Mattaj IW, Kay LE, Neuhaus D & Varani G (2000) The NMR structure of the 38 kDa U1A protein – PIE RNA complex reveals the basis of cooperativity in regulation of polyadenylation by human U1A protein. *Nature Structural Biology* **7**, 329–335.

30 Iwahara J, Anderson DE, Murphy EC & Clore GM (2003) EDTA-derivatized deoxythymidine as a tool for rapid determination of protein binding polarity to DNA by intermolecular paramagnetic relaxation enhancement. *J Am Chem Soc* **125**, 6634–6635.

31 Ueda T, Kato A, Ogawa Y, Torizawa T, Kuramitsu S, Iwai S, Terasawa H & Shimada I (2004) NMR study of repair mechanism of DNA photolyase by FAD-induced paramagnetic relaxation enhancement. *J Biol Chem* **279**, 52574–52579.

32 Roosild TP, Greenwald J, Vega M, Castronovo S, Riek R & Choe S (2005) NMR structure of mistic, a membrane-integrating protein for membrane protein expression. *Science* **307**, 1317.

33 Bertoncini CW, Jung Y-S, Fernández CO, Hoyer W, Griesinger C, Jovin TM & Zweckstetter M (2005) Release of long-range tertiary interactions potentiates aggregation of natively unstructured a-synuclein. *Proc Natl Acad Sci USA* **102**, 1430–1435.

34 Dedmon MM, Lindorff-Larsen K, Christodoulou J, Vendruscolo M & Dobson CM (2005) Mapping long-range interactions in alpha-synuclein using spin-label NMR and ensemble molecular dynamics simulations. *J Am Chem Soc* **127**, 476–477.

35 Felitsky DJ, Lietzow MA, Dyson HJ & Wright PE (2008) Modeling transient collapsed states of an unfolded protein to provide insights into early folding events. *Proc Natl Acad Sci USA* **105**, 6278.

36 Song J, Guo LW, Muradov H, Artemyev NO, Ruoho AE & Markley JL (2008) Intrinsically disordered gamma-subunit of cGMP phosphodiesterase encodes functionally relevant transient secondary and tertiary structure. *Proc Natl Acad Sci U S A* **105**, 1505–1510.

37 Pan BB, Yang F, Ye Y, Wu Q, Li C, Huber T & Su XC (2016) 3D structure determination of a protein in living cells using paramagnetic NMR spectroscopy. *Chem Commun (Camb)* **52**, 10237–10240.

38 Muntener T, Haussinger D, Selenko P & Theillet FX (2016) In-cell protein structures from 2D NMR experiments. *J Phys Chem Lett.* **7**, 2821–2825.

39 Balayssac S, Bertini I, Bhaumik A, Lelli M & Luchinat C (2008) Paramagnetic shifts in solid-state NMR of proteins to elicit structural information. *Proc Natl Acad Sci USA* **105**, 17284–17289.

40 Luchinat C, Parigi G, Ravera E & Rinaldelli M (2012) Solid state NMR crystallography through paramagnetic restraints. *J Am Chem Soc* **134**, 5006–5009.

41 Sengupta I, Nadaud PS, Helmus JJ, Schwieters CD & Jaroniec CP (2012) Protein fold determined by paramagnetic magic-angle spinning solid-state NMR spectroscopy. *Nature Chem* **4**, 410–417.

42 Nadaud PS, Helmus JJ, Kall SL & Jaroniec CP (2009) Paramagnetic ions enable tuning of nuclear relaxation rates and provide long-range structural restraints in solid-state NMR of proteins. *J Am Chem Soc* **131**, 8108–8120.

43 Wang S, Munro RA, Kim SY, Jung K-H, Brown LS & Ladizhansky V (2012) Paramagnetic relaxation enhancement reveals oligomerization interface of a membrane protein. *J Am Chem Soc* **134**, 16995–16998.

44 Iwahara J & Clore GM (2006) Detecting transient intermediates in macromolecular binding by paramagnetic NMR. *Nature* **440**, 1227–1230.

45 Volkov AN, Worrall JAR, Holtzmann E & Ubbink M (2006) Solution structure and dynamics of the complex between cytochrome c and cytochrome c peroxidase determined by paramagnetic NMR. *Proc Natl Acad Sci USA* **103**, 18945–18950.

46 Xu X, Reinle W, Hannemann F, Konarev PV, Svergun DI, Bernhardt R & Ubbink M (2008) Dynamics in a pure encounter complex of two proteins studied by solution scattering and paramagnetic NMR spectroscopy. *J Am Chem Soc* **130**, 6395–6403.

47 Tang C, Iwahara J & Clore GM (2006) Visualization of transient encounter complexes in protein-protein association. *Nature* **444**, 383–386.

48 Tang C, Schwieters CD & Clore GM (2007) Open-to-close transition in apo maltose-binding protein observed by paramagnetic NMR. *Nature* **449**, 1078–1082.

49 Hansen DF, Westler WM, Kunze MBA, Markley JL, Weinhold F & Led JJ (2012) Accurate structure and dynamics of the metal-site of paramagnetic metalloproteins from NMR parameters using natural bond orbitals. *J Am Chem Soc* **134**, 4670–4682.

50 Tang C, Ghirlando R & Clore GM (2008) Visualization of transient ultra-weak protein self-association in solution using paramagnetic relaxation enhancement. *J Am Chem Soc* **130**, 4048–4056.

51 Tang C, Louis JM, Aniana A, Suh JY & Clore GM (2008) Visualizing transient events in amino-terminal autoprocessing of HIV-1 protease. *Nature* **455**, 693–696.

52 Baker KA, Hilty C, Peti W, Prince A, Pfaffinger PJ, Wider G, Wüthrich K & Choe S (2006) NMR-derived dynamic aspects of N-type inactivation of a Kv channel suggest a transient interaction with the T1 domain. *Biochemistry* **45**, 1663–1672.

53 John M, Pintacuda G, Park AY, Dixon NE & Otting G (2006) Structure determination of protein-ligand complexes by transferred paramagnetic shifts. *J Am Chem Soc* **128**, 12910–12916.

54 Jahnke W, Perez LB, Paris CG, Strauss A, Fendrich G & Nalin CM (2000) Second-site NMR screening with a spin-labeled first ligand. *J Am Chem Soc* **122**, 7394–7395.

55 Bertini I, Fragai M, Lee Y-M, Luchinat C & Terni B (2004) Paramagnetic metal ions in ligand screening: the Co^{II} matrix metalloproteinase 12. *Angew Chem Int Ed* **43**, 2254–2256.

56 Softley CA, Bostock MJ, Popowicz GM & Sattler M (2020) Paramagnetic NMR in drug discovery. *J Biomol NMR* **74**, 287–309.

57 Iwahara J, Tang C & Clore GM (2007) Practical aspects of ^1H transverse paramagnetic relaxation enhancement measurements on macromolecules. *J Magn Reson* **184**, 185–195.

58 Orton HW & Otting G (2018) Accurate electron–nucleus distances from paramagnetic relaxation enhancements. *J Am Chem Soc* **140**, 7688–7697.

59 Ma L, Jørgensen AMM, Sorensen GO, Ulstrup J & Led JJ (2000) Elucidation of the paramagnetic R1 relaxation of heteronuclei and protons in Cu(II) plastocyanin from *Anabaena variabilis*. *J Am Chem Soc* **122**, 9473–9485.

60 Suturina EA, Mason K, Geraldes C, Chilton NF, Parker D & Kuprov I (2018) Lanthanide-induced relaxation anisotropy. *Phys Chem Chem Phys* **20**, 17676–17686.

61 Parker D, Suturina EA, Kuprov I & Chilton NF (2020) How the ligand field in lanthanide coordination complexes determines magnetic susceptibility anisotropy, paramagnetic NMR shift, and relaxation behavior. *Acc Chem Res* **53**, 1520–1534.

62 Pintacuda G, Kaikkonen A & Otting G (2004) Modulation of the distance dependence of paramagnetic relaxation enhancements by CSA x DSA cross-correlation. *J M6agn Reson* **171**, 233–243.

63 John M, Park AY, Pintacuda G, Dixon NE & Otting G (2005) Weak alignment of paramagnetic proteins warrants correction for residual CSA effects in measurements of pseudocontact shifts. *J Am Chem Soc* **127**, 17190–17191.

64 Invernici M, Trindade IB, Cantini F, Louro RO & Piccioli M (2020) Measuring transverse relaxation in highly paramagnetic systems. *J Biomol NMR* **74**, 431–442.

65 Otting G (2010) Protein NMR using paramagnetic ions. *Annu Rev Biophys* **39**, 387–405.

66 Pintacuda G, Park AY, Keniry MA, Dixonj NE & Otting G (2006) Lanthanide labeling offers fast NMR approach to 3D structure determinations of protein-protein complexes. *J Am Chem Soc* **128**, 3696–3702.

67 Clore GM (2015) Practical aspects of paramagnetic relaxation enhancement in biological macromolecules. *Methods Enzymol* **564**, 485–497.

68 Madl T, Bermel W & Zangger K (2009) Use of relaxation enhancements in a paramagnetic environment for the structure determination of proteins using NMR spectroscopy. *Angew Chem Int Ed* **48**, 8259–8262.

69 Tang Y, Huang YJ, Hopf TA, Sander C, Marks DS & Montelione GT (2015) Protein structure determination by combining sparse NMR data with evolutionary couplings. *Nat Methods* **12**, 751–754.

70 Raman S, Lange OF, Rossi P, Tyka M, Wang X, Aramini J, Liu G, Ramelot TA, Eletsky A, Szyperski T *et al*, (2010) NMR structure determination for larger proteins using backbone-only data. *Science* **327**, 1014–1018.

71 Al-Hashimi HM, Valafar H, Terrell M, Zartler ER, Eidsness MK & Prestegard JH (2000) Variation of molecular alignment as a means of resolving orientational ambiguities in protein structures from dipolar couplings. *J Magn Reson* **143**, 402–406.

72 Kontaxis G, Delaglio F & Bax A (2005) Molecular fragment replacement approach to protein structure determination by chemical shift and dipolar homology database mining. *Methods Enzymol* **394**, 42–78.

73 Tian F, Valafar H & Prestegard JH (2001) A dipolar coupling based strategy for simultaneous resonance assignment and structure determination of protein backbones. *J Am Chem Soc* **123**, 11791–11796.

74 Yagi H, Pilla KB, Maleckis A, Graham B, Huber T & Otting G (2013) Three-dimensional protein fold determination from backbone amide pseudocontact shifts generated by lanthanide tags at multiple sites. *Structure* **21**, 883–890.

75 Bertini I, Donaire A, Jiménez B, Luchinat C, Parigi G, Piccioli M & Poggi L (2001) Paramagnetism-based versus classical constraints: an analysis of the solution structure of Ca Ln Calbindin D_{9k}. *J Biomol NMR* **21**, 85–98.

76 Barbieri R, Luchinat C & Parigi G (2004) Backbone-only protein solution structures with a combination of classical and paramagnetism-based constraints: a method that can be scaled to large molecules. *ChemPhysChem* **21**, 797–806.

77 Bird LJ, Saraiva IH, Park S, Calcada EO, Salgueiro CA, Nitschke W, Louro RO & Newman DK (2014) Nonredundant roles for cytochrome c2 and two high-potential iron-sulfur proteins in the photoferrotroph *Rhodopseudomonas palustris* TIE-1. *J Bacteriol* **196**, 850–858.

78 Rayment I, Wesenberg G, Meyer TE, Cusanovich MA & Holden HM (1992) Three-dimensional structure of the high-potential iron-sulfur protein isolated from the purple phototrophic bacterium Rhodocyclus tenuis determined and refined at 1.5 A resolution. *J Mol Biol* **228**, 672–686.

79 Stelter M, Melo AM, Hreggvidsson S, Saraiva LM, Teixeira M & Archer M (2010) Structure at 1.0 A resolution of a high-potential iron-sulfur protein involved in the aerobic respiratory chain of Rhodothermus marinus. *J Biol Inorg Chem* **15**, 303–313.

80 Dickson DPE, Johnson CE, Middleton P, Rush JD, Cammack R, Hall DO, Mullinger RN & Rao KK (1976) Mossbauer spectroscopic studies of iron-sulphur proteins with four-iron active centres. *J Physique Colloq* **37**, C6–171-C6-175.

81 Emptage MH, Kent TA, Huynh BH, Rawlings J, Orme-Johnson WH & Münck E (1980) Nature of the iron-sulfur centers in a ferredoxin from Azotobacter-

Vinelandii – Mossbauer studies and cluster displacement experiments. *J Biol Chem* **255**, 1793–1796.

82 Blondin G & Girerd J-J (1990) Interplay of electron exchange and electron transfer in metal polynuclear complexes in proteins or chemical models. *Chem Rev* **90**, 1359–1376.

83 Garcia-Serres R, Clemancey M, Latour JM & Blondin G (2018) Contribution of Mossbauer spectroscopy to the investigation of Fe/S biogenesis. *J Biol Inorg Chem* **23**, 635–644.

84 Mouesca J-M & Lamotte B (1998) Iron-Sulfur clusters and their electronic and magnetic properties. *Coord Chem Rev* **178–180**, 1573–1614.

85 Noodleman L, Case DA, Mouesca J-M & Lamotte B (1996) Valence electron delocalization in polynuclear iron-sulfur clusters. *JBIC* **1**, 177–182.

86 Bertini I, Capozzi F, Eltis LD, Felli IC, Luchinat C & Piccioli M (1995) Sequence specific assignment of ligand cysteine protons of oxidized, recombinant HiPIP I from *Ectothiorhodospira halophila*. *Inorg Chem* **34**, 2516–2523.

87 Hagen WR.(2008) Biomolecular EPR spectroscopy. CRC Press, Boca Raton, FL.

88 Bertini I, Cowan JA, Luchinat C, Natarajan K & Piccioli M (1997) Characterization of a partially unfolded high potential iron protein relevant to the folding pathway and cluster stability. *Biochemistry* **36**, 9332–9339.

89 Banci L, Camponeschi F, Ciofi-Baffoni S & Piccioli M (2018) The NMR contribution to protein-protein networking in Fe-S protein maturation. *J Biol Inorg Chem* **23**, 687.

90 Machonkin TE, Westler WM & Markley JL (2002) $^{13}C–^{13}C$ 2D NMR: a novel strategy for the study of paramagnetic proteins with slow electronic relaxation times. *J Am Chem Soc* **124**, 3204–3205.

91 Ciofi-Baffoni S, Gallo A, Muzzioli R & Piccioli M (2014) The IR-N-15-HSQC-AP experiment: a new tool for NMR spectroscopy of paramagnetic molecules. *J Biomol NMR* **58**, 123–128.

92 Trindade IB, Invernici M, Cantini F & Louro RO (2020) Piccioli M (2020) Sequence-specific assignments in NMR spectra of paramagnetic systems: a non-systematic approach. *Inorg Chim Acta* **514**, 119984.

93 Trindade IB, Invernici M, Cantini F, Louro RO & Piccioli M. (2020) (1)H, (13)C and (15)N assignment of the paramagnetic high potential iron-sulfur protein (HiPIP) PioC from Rhodopseudomonas palustris TIE-1. *Biomol Nmr Assign* **14**, 211–215.

94 Banci L, Bertini I, Eltis LD, Felli IC, Kastrau DHW, Luchinat C, Piccioli M, Pierattelli R & Smith M (1994) The three dimensional structure in solution of the paramagnetic protein high-potential iron-sulfur

protein I from *Ectothiorhodospira halophila* through nuclear magnetic resonance. *Eur J Biochem* **225**, 715–725.

95 Bertini I, Capozzi F, Luchinat C, Piccioli M & Vila AJ (1994) The Fe4S4 centers in ferredoxins studied through proton and carbon hyperfine coupling. Sequence specific assignments of cysteines in ferredoxins from Clostridium acidi urici and *Clostridium pasteurianum*. *J Am Chem Soc*. **116**, 651–660.

96 Lin IJ, Gebel EB, Machonkin TE, Westler WM & Markley JL (2005) Changes in hydrogen-bond strenght explain reduction potentials in 10 ruvredoxin variants. *Proc Natl Acad Sci USA* **102**, 14581–14586.

97 Bertini I, Luchinat C, Parigi G & Ravera E. (2016) NMR of Paramagnetic Molecules. Elsevier.

98 Yang J, Anishchenko I, Park H, Peng Z, Ovchinnikov S & Baker D (2020) Improved protein structure prediction using predicted interresidue orientations. *Proc Natl Acad Sci U S A* **117**, 1496–1503.

99 Cong Q, Anishchenko I, Ovchinnikov S & Baker D (2019) Protein interaction networks revealed by proteome coevolution. *Science* **365**, 185–189.

100 Senior AW, Evans R, Jumper J, Kirkpatrick J, Sifre L, Green T, Qin C, Zidek A, Nelson AWR, Bridgland A *et al*, (2020) Improved protein structure prediction using potentials from deep learning. *Nature* **577**, 706–710.

101 Grime GW, Zeldin OB, Snell ME, Lowe ED, Hunt JF, Montelione GT, Tong L, Snell EH & Garman EF (2020) High-throughput PIXE as an essential quantitative assay for accurate metalloprotein structural analysis: development and application. *J Am Chem Soc* **142**, 185–197.

102 Lopez-Mendez B & Guntert P (2006) Automated protein structure determination from NMR spectra. *J Am Chem Soc* **128**, 13112–13122.

103 Kim JD, Pike DH, Tyryshkin AM, Swapna GVT, Raanan H, Montelione GT, Nanda V & Falkowski PG (2018) Minimal heterochiral de novo designed 4Fe-4S binding peptide capable of robust electron transfer. *J Am Chem Soc* **140**, 11210–11213.

104 Lombardi A, Pirro F, Maglio O, Chino M & DeGrado WF (2019) De novo design of four-helix bundle metalloproteins: one scaffold, diverse reactivities. *Acc Chem Res* **52**, 1148–1159.

105 Nanda V, Senn S, Pike DH, Rodriguez-Granillo A, Hansen WA, Khare SD & Noy D (2016) Structural principles for computational and de novo design of 4Fe-4S metalloproteins. *Biochim Biophys Acta* **1857**, 531–538.

106 Keller R & Wüthrich K (2002) Optimizing the process of nuclear magnetic resonance spectrum analysis and

computer aided resonance assignment. Thèse de doctorat, ETH Zurich, Switzerland.

107 Güntert P (2004) Automated NMR structure calculation with CYANA. *Methods Mol Biol* **278**, 353–378.

108 Guntert P & Buchner L (2015) Combined automated NOE assignment and structure calculation with CYANA. *J Biomol NMR* **62**, 453–471.

109 Case DA, Ben-Shalom IY, Brozell SR, Cerutti DS, Cheatham TE III, Cruzeiro VWD, Darden TA, Duke RE, Ghoreishi D, Gilson MK *et al.* (2018) AMBER 2018. University of California, San Francisco, CA.

110 Carvalho AT & Swart M (2014) Electronic structure investigation and parametrization of biologically relevant iron-sulfur clusters. *J Chem Inf Model* **54**, 613–620.

111 Karmi O, Marjault HB, Pesce L, Carloni P, Onuchic JN, Jennings PA, Mittler R & Nechushtai R (2018) The unique fold and lability of the [2Fe-2S] clusters of NEET proteins mediate their key functions in health and disease. *J Biol Inorg Chem* **23**, 599–612.

112 Tejero R, Snyder D, Mao B, Aramini JM & Montelione GT (2013) PDBStat: a universal restraint converter and restraint analysis software package for protein NMR. *J Biomol NMR* **56**, 337–351.

113 Bhattacharya A, Tejero R & Montelione GT (2007) Evaluating protein structures determined by structural genomics consortia. *Prot Struct Funct Bioinformat* **66**, 778–795.

Supporting information

Additional supporting information may be found online in the Supporting Information section at the end of the article.

Table S1. List of experiments collected to perform the sequence specific assignment and the structure calculations.

Table S2. List of experiments optimized to identify fast relaxing resonances.

Table S3. Relaxation rates, measured at 298K, 500 MHz, of 1H signals in PioC.

Table S4. Upper limit distances obtained from PREs used for structure calculations.

Table S5. Summary of restraints and structure quality factors of the structure families obtained after molecular dynamics refinement (AMBER-16).

Table S6. Pairwise RMSD to the mean for PioC structures obtained with different sets of restraints.

Text S1. Definition of the cluster.

Text S2. Structure calculations and refinement.

Text S3. ^{1}H R_1 and R_2 relaxation measurements and PRE constraints.

Text S4. References.

Fig. S1. 1D ^{1}H NMR spectrum of PioC, optimized to observe hyperfine shifted and fast relaxing resonances and 1D NOE difference spectra.

Fig. S2. Experimental ^{15}N R_1, R_2 rates and heteronuclear NOEs as obtained from the ^{15}N relaxation experiments performed at 500 MHz, 298K on a ^{15}N labeled PioC sample.